



Transport mechanism of urban plume dispersion

Ziwei Mo, Chun-Ho Liu*

Department of Mechanical Engineering, The University of Hong Kong, Hong Kong



ARTICLE INFO

Keywords:
 Aerodynamic resistance
 Plume dispersion
 Tracer flux
 Urban area
 Wind tunnel experiment

ABSTRACT

Winds (advection) and turbulence (diffusion) are the driving forces for urban plume dispersion whose partitioning is complicated by urban morphology and the conditions of atmospheric surface layer (ASL). Wind tunnel parametric tests are conducted to examine the plume behavior in the turbulent boundary layers (TBLs) over hypothetical buildings (roughness elements of ribs and bricks) with drag coefficient $C_d (= 2u_r^2/U_\infty^2)$, where u_r and U_∞ are, respectively, the friction velocity and the freestream velocity) varying from 4.7×10^{-3} to 10×10^{-3} . Vehicular emission is modeled by atomizing water vapor via a ground-level line source in crossflows. The laboratory measurements show that the mean tracer concentrations $\bar{\psi}$ exhibit the theoretical Gaussian form, supporting the classic plume dispersion framework. The horizontal advection tracer flux $\bar{u} \bar{\psi}$ dominates the transport processes compared with the vertical turbulent tracer flux $\bar{w}'\bar{\psi}'$. Increasing C_d leads to a decrease in $\bar{u} \bar{\psi}$ and an increase in $\bar{w}'\bar{\psi}'$ simultaneously, and vice versa. The changes in partitioning of transport processes in response to urban morphology imply that the conventional parameterization of dispersion coefficient σ_z (determined by atmospheric stability only) should be applied cautiously for urban setting. A new simple scheme of σ_z parameterization, which specifically accounts for the influence from urban roughness on the plume dispersion, is proposed.

1. Introduction

Degrading urban air quality has attracted public concern owing to the drawback on life quality [1,2]. The health risk could be caused by the short-term exposure to elevated concentrations of hazardous contaminants or the long-term exposure to ambient pollutants [3,4]. Although regulation has been enacted to abate emissions and accidental release of harmful materials, air pollution episodes have frequently occurred that threaten the general public [5,6]. Promoting wind breeze and pedestrian-level ventilation facilitates pollutant dispersal [7,8]. However, massive, irregular building clusters complicate the winds and turbulence in the atmospheric surface layers (ASLs) over compact, dense cities that pose a challenge to environmentalists [9,10]. In view of the flow inhomogeneity, the conventional Gaussian plume model handling pollutant dispersion over open terrain is no longer applicable to urban setting [11]. Understanding the mechanism of pollutant dispersion in response to urban morphology is therefore essential to effectuate the mitigation [12–14].

Influence of urban morphology on ASL wind, turbulence and transport processes has been extensively studied. Wind tunnel experiments have been used to test the sensitivity of the dynamics to

boundary conditions (BCs) in a fully controllable manner [15,16]. A few geometric parameters in hypothetical configuration, such as aspect (building-height-to-street-width) ratio AR , plan area index γ_P ($= A_p/A_T$; where A_p and A_T are the plan area and the total area, respectively) and frontal area index γ_F ($= A_F/A_T$; where A_F is the frontal area), are indicators commonly employed to evaluate the performance of pedestrian-level ventilation and pollutant disposal over idealized urban models fabricated by ribs [17] and cubes [18]. To test the response of flows to surface roughness, aerodynamic parameters, for instance, the zero-plane displacement height d and the roughness length z_0 derived by the logarithmic law of the wall (log-law), are examined over a range of configurations. For example, cases of $0.08 \leq AR \leq 0.5$ [19] and $0.5 \leq AR \leq 2$ [20], covering the skimming flow regime, wake interference regime, and isolated roughness regime, have been attempted. Sensitivity to γ_F and γ_P has been conducted as well for $0.06 \leq \gamma_F = \gamma_P \leq 0.25$ [21], $0.04 \leq \gamma_F = \gamma_P \leq 0.39$ [22] together with $0.09 \leq \gamma_F \leq 0.24$ and $0.11 \leq \gamma_P \leq 0.24$ [23].

In isothermal, laboratory wind-tunnel experiments, the turbulence is produced by mechanical wind shear but not buoyancy. The roughness length z_0 was determined as a function of γ_F and γ_P compared with empirical approaches [24,25]. Similarly, the zero-plane displacement

* Corresponding author. Department of Mechanical Engineering, The University of Hong Kong, 7/F, Haking Wong Building, Pokfulam Road, Hong Kong.
 E-mail address: liuchunho@graduate.hku.hk (C.-H. Liu).

URL: <https://aplhk.tech> (C.-H. Liu).

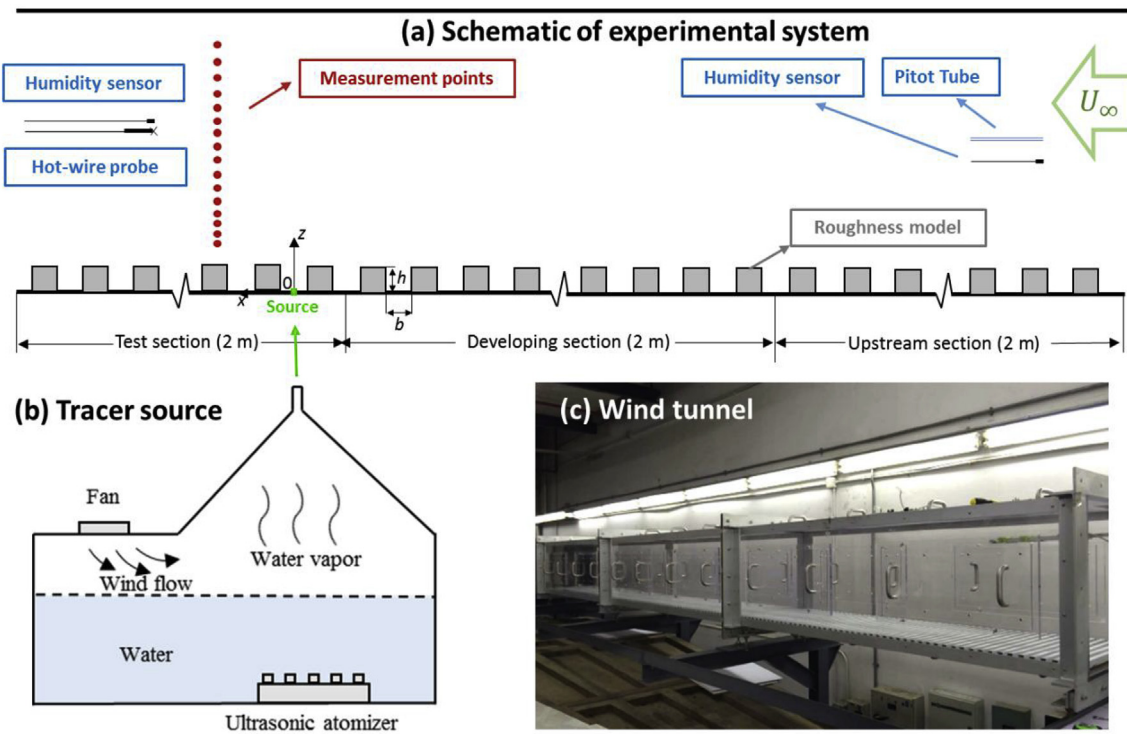


Fig. 1. Schematic of (a) experimental setup, (b) tracer source and (c) wind tunnel infrastructure.

height d was estimated by the regression of the log-law to the experimental data collected from laboratory [26] or field [27] measurements. Pedestrian-level ventilation and pollutant disposal were also contrasted over different configurations of building cluster [28–30]. The plume dispersion over rough surfaces after a ground-level source was characterized as well [31–33].

Apart from idealized urban roughness, reduced-scale physical models of realistic urban setting have been employed in wind tunnel experiments. Development of turbulent boundary layer (TBL) [34], flow dynamics [35] and tracer dispersion [36] were investigated. However, real urban morphology consists of diversified building types with wide spectra of size and shape that are highly irregular and randomly distributed. Under this circumstance, it is too complicated, if not impossible, to measure the geometric parameters such as AR , γ_F and/or γ_P . Indeed, it is unnecessary to calculate all the flow details for practical problems [37]. Hence, the indicators of aerodynamic resistance were employed to parameterize the effect of urban morphology on pedestrian-level ventilation and pollutant plume dispersion in built environment. The dimensionless number, drag coefficient

$$C_d = \frac{2u_r^2}{U_\infty^2}, \quad (1)$$

quantifies the resistance induced by solid boundaries [38,39] where U_∞ is the freestream wind speed (m sec^{-1}), $u_r (= (\tau_w/\rho)^{1/2})$ the friction velocity (m sec^{-1}), ρ the fluid density (kg m^{-3}) and τ_w the stress (Pa). It is defined analogously to skin-friction coefficient C_f [40] and friction factor f [41] which are indicators commonly employed in wind engineering and building projects.

In our previous studies, the drag coefficient has been employed to parameterize pedestrian-level ventilation [42] and plume spread [43]. The solution framework was validated based on ribs only [44]. In this connection, this study is conceived to examine the plume spread over the roof level of buildings and verify the newly proposed analytical formulation of dispersion coefficient σ_z using arrays of both rib-type and brick-type roughness elements by wind tunnel experiments. Water vapor is atomized through a ground-level line source in crossflows to

model vehicular emission. Humidity sensors are used to probe the tracer concentrations while X-type constant-temperature (CT) hot-wire anemometers (HWA) are used to measure the velocities. Apart from the mean concentrations, the tracer fluxes, which are calculated based on the Reynolds analogy and the anti-gradient diffusion model, are contrasted to elucidate the plume transport mechanism over hypothetical urban areas. This section outlines the problems and reviews the literature. The theoretical background is derived in Section 2. Afterward, Section 3 presents the methodology. The results obtained are then discussed in Section 4. Section 5 concludes the study.

2. Theoretical background

2.1. Tracer fluxes

Take the steady-state plume dispersion after an infinite (in the spanwise direction y), horizontal line source perpendicular to the TBL flows as an example, the tracer transport on the vertical ($x-z$; where x and z are the streamwise and vertical directions, respectively) plane is governed by mass conservation

$$\frac{\partial}{\partial x} \bar{u} \bar{\psi} = - \frac{\partial}{\partial z} \overline{w''\psi''} \quad (2)$$

where \bar{u} denotes the mean-wind speed, $\bar{\psi}$ the mean tracer concentration, $\bar{u} \bar{\psi}$ the (horizontal) advection tracer flux and $\overline{w''\psi''}$ the (vertical) turbulence tracer flux. Here, the overbar $\bar{\phi}$ signifies the mean properties averaged in time and the double prime $\phi'' (= \phi - \bar{\phi})$ the deviation from the mean. It is assumed that the spanwise/vertical mean flows are small compared with their streamwise counterpart. Moreover, the streamwise turbulence tracer flux $\overline{u''\psi''}$ is negligible compared with its mean component $\bar{u} \bar{\psi}$ [45]. The (two-dimensional; 2D) tracer transport behind a line source in crossflows is therefore essentially the balance between the tracer fluxes governed by streamwise advection and vertical diffusion. In the light of mixing-length theory and anti-gradient diffusion model, it is assumed that the vertical turbulent tracer flux is estimated by the mean concentration gradient, that is

Table 1
Properties of the rough-surface flows measured in the wind tunnel experiments.

| Measurement Cases | Ribs | | Bricks | | | | | | | | | | | | |
|---|--|-------|--------|--------|---|--------|--------|--------|--|---------|---------|-------|---|-----------|-----------|
| | Low Wind Speed ($U_\infty \approx 3 \text{ m s}^{-1}$) | | | | High Wind Speed ($U_\infty \approx 6 \text{ m s}^{-1}$) | | | | Low Wind Speed ($U_\infty \approx 3 \text{ m s}^{-1}$) | | | | High Wind Speed ($U_\infty \approx 6 \text{ m s}^{-1}$) | | |
| | LS | LS | LS | LS 1/8 | LS 1/12 | HS 1/2 | HS 1/4 | HS 1/8 | HS 1/12 | LS h:21 | LS h:41 | LS | LS 3:h:41 | HS 2:h:41 | HS 3:h:41 |
| Obstacle [$\times 10^{-3} \text{ m}$] | 19 | 19 | 19 | 19 | 19 | 152 | 228 | 322 | 11 | 23 | 34 | 11 | 23 | 34 | 34 |
| TBL thickness | 38 | 76 | 152 | 228 | 38 | 76 | 152 | 228 | 64 | 64 | 32 | 32 | 64 | 64 | 34 |
| δ [$\times 10^{-3} \text{ m}$] | 259 | 279 | 304 | 284 | 264 | 265 | 285 | 260 | 166 | 176 | 193 | 199 | 171 | 198 | 204 |
| Free-stream wind speed | 3.3 | | | | 6.7 | 6.6 | 6.7 | 6.6 | 3.3 | 3.5 | 3.4 | 3.3 | 6.6 | 6.7 | 6.5 |
| U_∞ [m sec^{-1}] | 0.18 | 0.22 | 0.38 | 0.45 | 0.47 | 0.45 | 0.47 | 0.48 | 0.16 | 0.18 | 0.19 | 0.20 | 0.32 | 0.34 | 0.39 |
| Friction velocity u_r [m sec^{-1}] | 0.055 | 0.067 | 0.057 | 0.068 | 0.070 | 0.068 | 0.070 | 0.070 | 0.048 | 0.051 | 0.056 | 0.061 | 0.048 | 0.051 | 0.060 |
| u_r/U_∞ | 6.3 | 8.5 | 9.4 | 9.3 | 6.6 | 9.2 | 10 | 4.8 | 5.2 | 6.1 | 7.0 | 4.7 | 5.2 | 6.2 | 7.1 |
| Drag coefficient | $C_d (= 2u_r^2/U_\infty^2)$ [$\times 10^{-3}$] | | | | | | | | | | | | | | |
| Reynolds number [$\times 10^3$] | 79 | 86 | 93 | 84 | 163 | 175 | 191 | 168 | 54 | 61 | 66 | 67 | 113 | 121 | 126 |
| $Re_r (= \mu u_r \delta / \mu)$ | 4 | 5 | 6 | 9 | 12 | 13 | 12 | 12 | 3 | 4 | 4 | 6 | 7 | 7 | 8 |
| Displacement height d/h | 0.24 | 0.23 | 0.37 | 0.13 | 0.12 | 0.27 | 0.10 | 0.34 | 0.26 | 0.11 | 0.05 | 0.25 | 0.24 | 0.11 | 0.08 |
| Roughness length z_0/h [$\times 10^{-3}$] | 17 | 30 | 50 | 53 | 21 | 38 | 56 | 63 | 11 | 16 | 15 | 12 | 16 | 17 | 15 |

$$\overline{w''\psi''} = -K_z \times \partial \bar{\psi} / \partial z \quad (3)$$

where K_z is the eddy diffusivity of mass. The Reynolds analogy

$$K_z = \alpha K_m \quad (4)$$

is commonly employed to estimate the eddy diffusivity of mass according to its momentum counterpart K_m . In turbulent flows, α is a constant close to unity [3].

2.2. Dispersion coefficient

The mean tracer concentrations on the vertical x - z plane can be calculated by

$$\bar{\psi}(x, z) = \frac{\dot{q}}{\sqrt{2\pi U \sigma_z}} \left\{ \exp \left[-\frac{(z - z_s)^2}{2\sigma_z^2} \right] + \exp \left[-\frac{(z + z_s)^2}{2\sigma_z^2} \right] \right\}. \quad (5)$$

Here, U is the mean-wind speed, z_s the plume center height and \dot{q} the tracer emission per unit source length per unit time [46]. Plume rise is not considered in this paper so z_s is equal to the emission height. Several schemes of the (vertical) dispersion coefficient σ_z have been developed in terms of atmospheric stability and the downwind distance after the source x , e.g., Pasquill–Gifford stability classes [46,47]. The Briggs formula and its modification for the dispersion coefficients of Gaussian plume model were developed to account for urban effect [48–50]. Other parameterizations have been attempted in the development of pollutant dispersion models for urban setting [51,52]. However, they have been only calibrated empirically based on the field observation of a few cities that hardly handled the broad spectra of urban morphology. Practical diffusion models, such as Industrial Source Complex Version 3 (ISC3) focused on how atmospheric stability and complex terrain affect the plume dispersion [53]. Similarly, dispersion over urban boundary layer was included in the American Meteorological Society (AMS) Environmental Protection Agency (EPA) Regulatory Model (AERMOD) in which the effect on ASL was mainly measured in terms of urban heat flux rather than urban morphology [54]. Building geometry, such as height, separation and frontal areas, were used by the Atmospheric Dispersion Modelling System Urban (ADMS-Urban) to predict the street-level pollutant concentrations [55]. CALPUFF employed the non-steady-state puff dispersion to calculate plume dispersion in which building downwash was used to modify the plume rise [56]. The effect of urban morphology on the plume dispersion at district scale (~km) was barely considered by ADMS-Urban or CALPUFF. SIRANE, on the other hand, adopted the street network to calculate street-canyon pollutant concentrations [57,58]. The pollutant dispersion over roof level was determined by the Gaussian model based on the Pasquill-Gifford stability classes [46,47].

Recently, a new analytical formulation of vertical dispersion coefficient was proposed in which the drag coefficient C_d was used to handle the influence of (hypothetical) urban areas on the plume dispersion aloft [33]. Analogous to the classic K -theory, anti-gradient diffusion model was used to describe the dispersion coefficient

$$\sigma_z = \sqrt{2K_z \times x/U_\infty} \quad (6)$$

in which the eddy diffusivity of mass K_z ($= l_* u_*$) is the product of the characteristic scales of length l_* and velocity u_* . The characteristic length scale is proportional to the elevation that is in the form $l_* = \kappa z$ where κ ($= 0.4$) is the von Kármán constant and z the wall-normal distance [59]. The dispersion coefficient was then expressed as $\sigma_z = (2 \kappa u_* z x/U_\infty)^{1/2}$. It is noteworthy that the emission height z_s could be used instead of height z for plume dispersion application. It is thus a spatial function in terms of both streamwise and vertical locations that is different from the conventional Gaussian-model framework. Moreover, the parameterization is applicable to ASL only in which the dispersion coefficients are largely influenced by the surface roughness but not atmospheric stabilities.

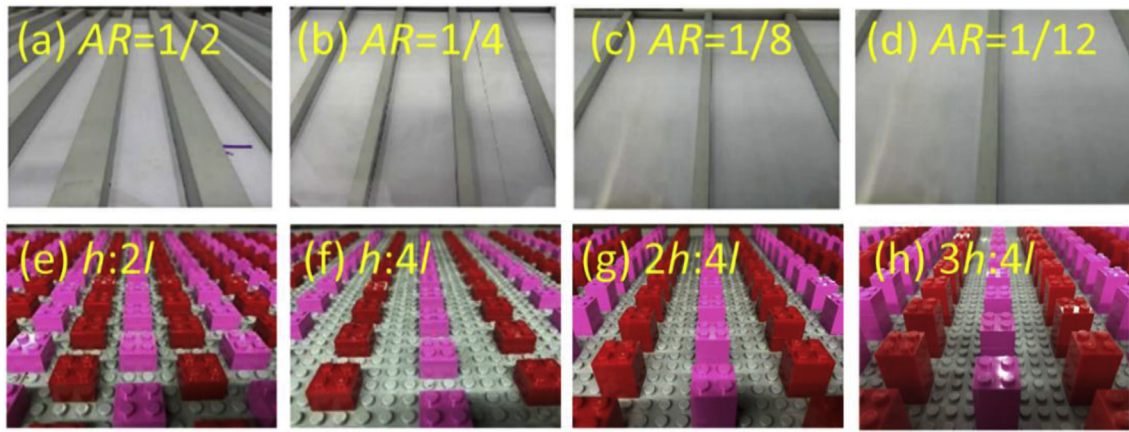


Fig. 2. Arrays of roughness elements in the form of ribs: (a) $AR = 1/2$, (b) $AR = 1/4$, (c) $AR = 1/8$, and (d) $AR = 1/12$; and bricks: (e) $h:2l$, (f) $h:4l$, (g) $2h:4l$, and (h) $3h:4l$.

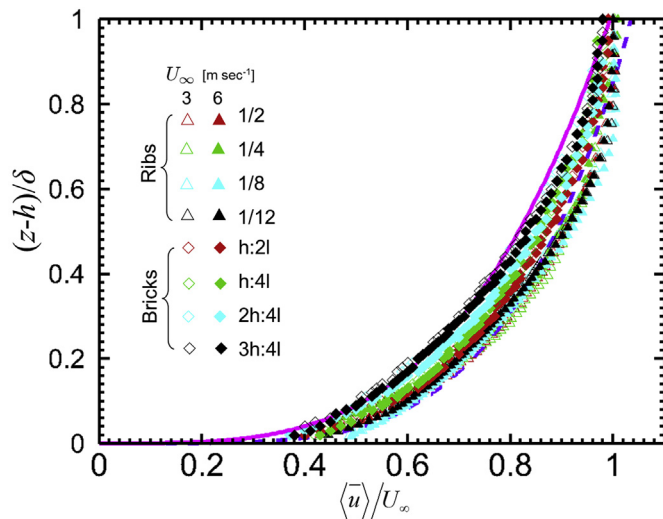


Fig. 3. Dimensionless mean-wind speeds $\langle \bar{u} \rangle / U_\infty$ over ribs and bricks plotted against dimensionless height $(z-h)/\delta$. Also shown is the power-law fitting Equation (9) with $n = 0.21$ (magenta solid line) and $n = 0.28$ (purple dashed line).

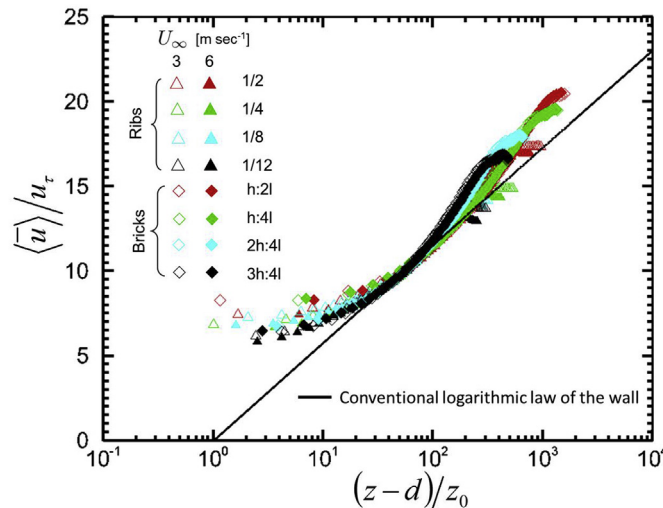


Fig. 4. Dimensionless mean-wind speeds $\langle \bar{u} \rangle / u_\tau$ over ribs and bricks plotted against dimensionless height $(z-d)/z_0$ in semi-logarithmic scale.

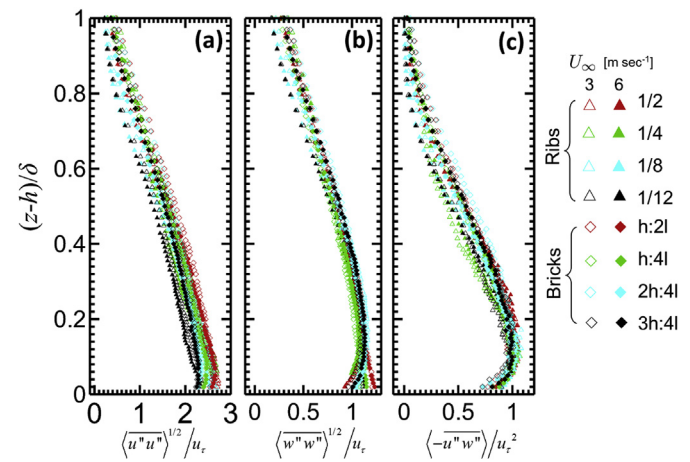


Fig. 5. Dimensionless turbulence properties of (a) streamwise fluctuating velocity $\langle \bar{u}' \bar{u}'' \rangle^{1/2} / u_\tau$, (b) vertical fluctuating velocity $\langle \bar{w}' \bar{w}'' \rangle^{1/2} / u_\tau$ and (c) turbulent momentum flux $\langle -\bar{u}' \bar{w}'' \rangle / u_\tau^2$ over ribs and bricks plotted against dimensionless height $(z-h)/\delta$.

Indeed, the transport over rough surfaces are dominated by the large, energy-carrying motion scales [60]. The characteristic length scale and the TBL thickness are therefore comparable $l_* \approx \delta$ from the transport point of view. Whereas, it is noteworthy that the approximation is valid in the intermediate-to far field only so near-field inaccuracy exists [3]. Further studies are needed to quantify the uncertainty and its influence on the pollutant transport. Nonetheless, it does not affect much the plume dispersion parameterization. Equation (6) is then simplified to yield the functional form of dispersion coefficient

$$\sigma_z \propto x^{1/2} \times \delta^{1/2} \times C_d^{1/4}. \quad (7)$$

The influence of urban areas on pollutant transport is therefore measured by the drag coefficient C_d (Equation (1)), i.e. the drag coefficient is directly proportional to the square of friction velocity. We use the TBL thickness δ for scaling, Equation (7) in turn arrives the following dimensionless form

$$\sigma_z / \delta \propto (x/\delta)^{1/2} \times C_d^{1/4}. \quad (8)$$

The above parameterization signifies that σ_z is a function of C_d and x but independent from z that fits into the conventional Gaussian-model framework for intermediate-to far-field estimates. It can be applied to a shorter range by expressing l_* as a spatial function of z or z_s . The mean tracer concentrations, however, do not follow Equation (5) anymore. As

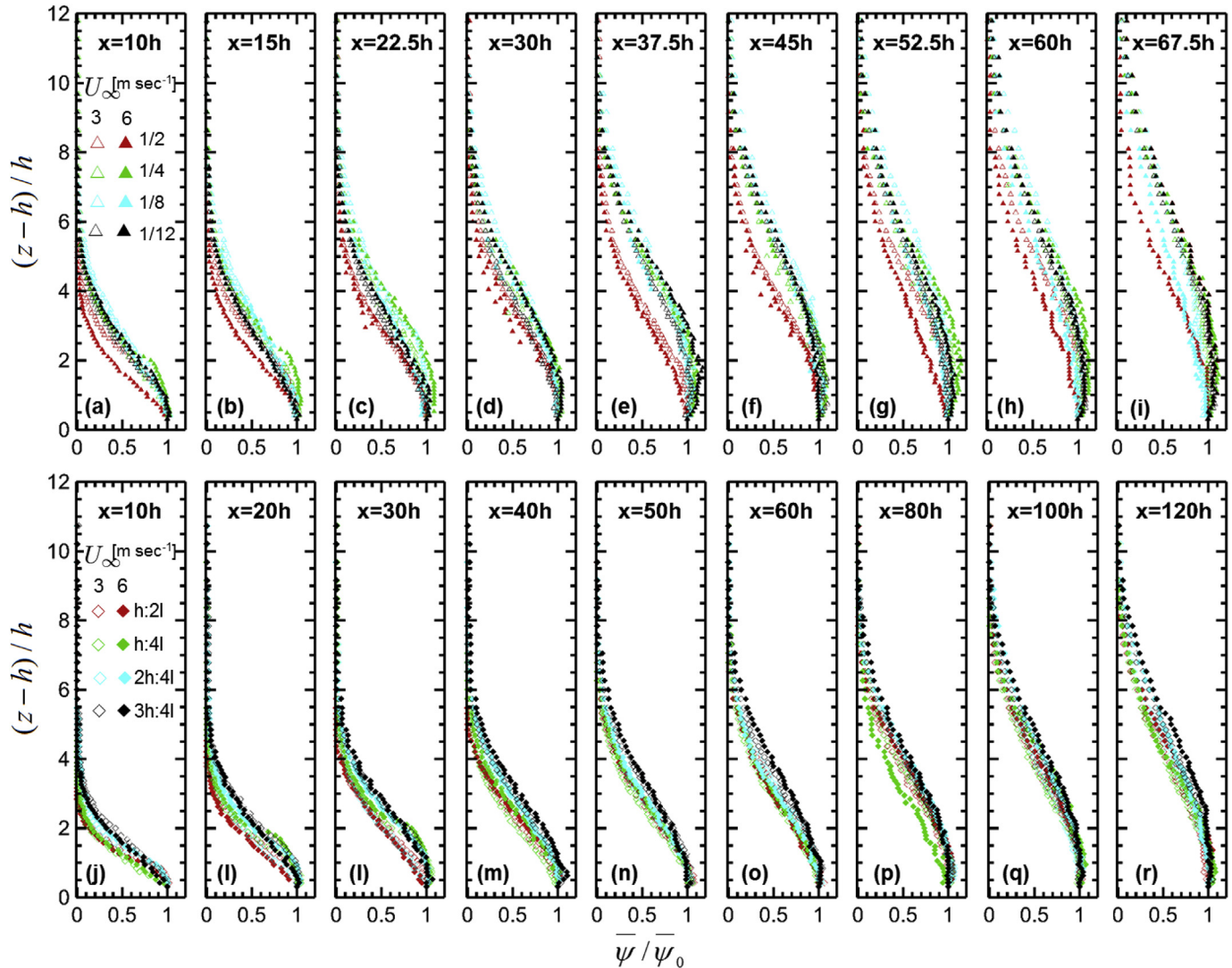


Fig. 6. Dimensionless tracer concentrations $\bar{\psi}/\bar{\psi}_0$ over ribs (a to i) and bricks (j to r) plotted against dimensionless height $(z-h)/h$ at different streamwise locations x .

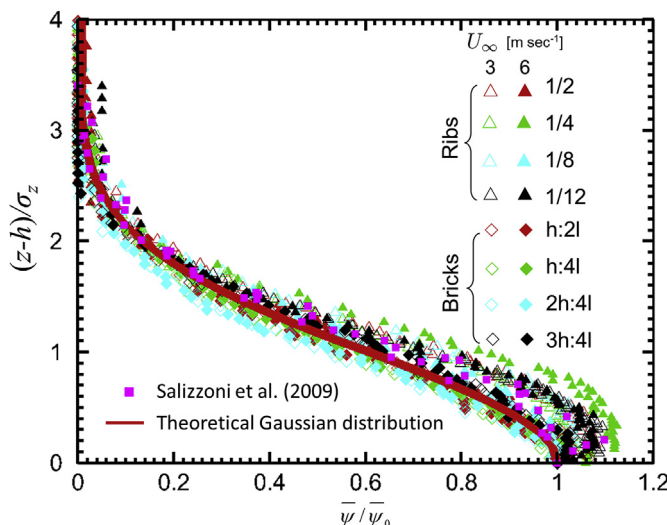


Fig. 7. Dimensionless tracer concentrations $\bar{\psi}/\bar{\psi}_0$ plotted against dimensionless height $(z-h)/\sigma_z$ at streamwise location $x = 60h$.

a preliminary study, a simple characteristic length scale $l_* \approx \delta$ is assumed in this paper. More sophisticated expressions of characteristic length scale will be tested in the future to improve the parameterization. It is also noted that modern, more complex dispersion models depend on the height in the ASL, Equation (8) is therefore an intermediate, simpler proposal of the parameterization of dispersion coefficient. Additional studies are needed to improve its functionality.

3. Methodology

3.1. Laboratory wind tunnel

Experiments of reduced-scale physical models are conducted in the wind tunnel (length 6 m × width 0.56 m × height 0.56 m) in our laboratory (Fig. 1). The flows are driven by a blower in which the wind speeds (0.5 m s⁻¹ to 12 m s⁻¹) are adjusted by a frequency inverter. The background turbulence level is suppressed to less than 5% collectively by a flow straightener, a settling chamber, a contraction cone and a honeycomb screen. Roughness elements are installed on the entire 6-m floor, generating fully-developed TBLs. Measurements are conducted at two levels of flow (low 3 m s⁻¹ and high 6 m s⁻¹ winds) to test the dependence on the Reynolds number Re_∞ ($= \rho U_\infty \delta / \mu$; where μ is the dynamic viscosity of air) which is over 10^4 (Table 1) to minimize the viscous effect on the transport. A traverse system is installed for sensor

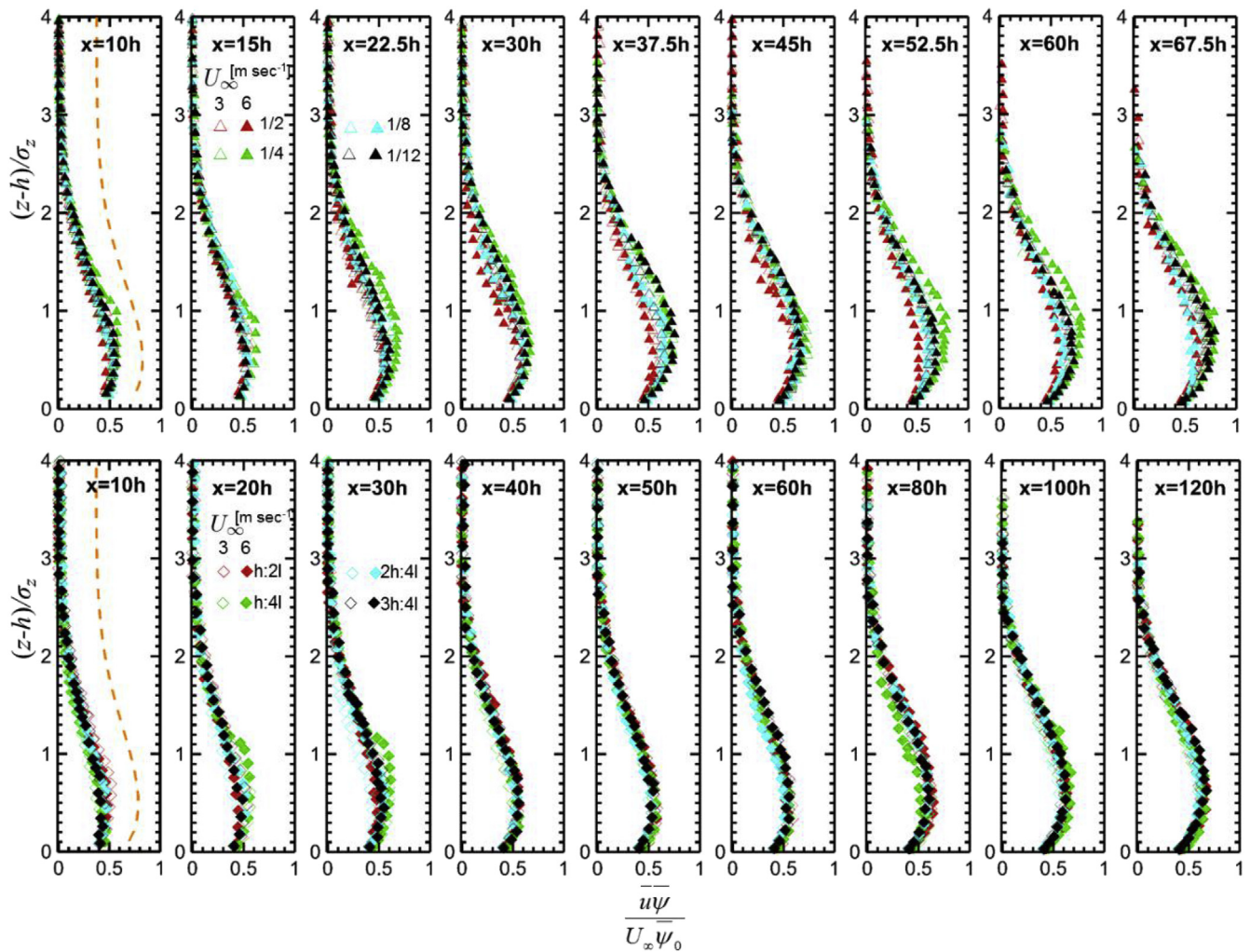


Fig. 8. Dimensionless advection tracer flux $\bar{u} \bar{\psi} / U_\infty \bar{\psi}_0$ over ribs (a to i) and bricks (j to r) plotted against dimensionless height $(z-h)/h$ at different streamwise locations x . Orange dashed lines depict the theoretical variation (Equation (11)).

probing at 1-mm spatial resolution. Details of the wind tunnel instrumentation were reported elsewhere [61,62].

3.2. Roughness elements

The hypothetical urban areas are modeled by two types of roughness element (Fig. 2). Identical square aluminium bars (size $h = 19$ mm), which denote rib-type roughness elements, are assembled to simulate idealized street canyons. The bars span the entire width ($L = 0.56$ m) of the wind tunnel floor. Besides, obstacle blocks, which denote brick-type roughness elements, are fabricated by staggering LEGO® bricks. Each LEGO® brick has dimensions l (length 16 mm) $\times l$ (width 16 mm) $\times h$ (height 11.4 mm, including the brick studs). The surface roughness, which influences the aerodynamic resistance directly, is adjusted by varying the space b between the bars or bricks in streamwise direction and/or mounting additional bricks on the top.

Four cases of rib-type roughness elements, whose $AR = 1/2, 1/4, 1/8$ and $1/12$, are adopted. Another four cases of brick-type roughness elements, which are arranged in obstacle-height-to-separation ratio $h:2l, h:4l, 2h:4l$ (double-layer LEGO® bricks) and $3h:4l$ (triple-layer LEGO® bricks), are considered as well. Totally, eight roughness configurations are examined whose drag coefficients are in the range of $4.7 \times 10^{-3} \leq C_d \leq 10 \times 10^{-3}$ ($0.048 \leq u_r/U_\infty \leq 0.071$) (Table 1).

3.3. Tracer source

A tracer line source, which overlaps the (crosswind) centerline of the full-span ground surface of one of the street canyons, is simulated by atomizing water vapor in a tank under the wind-tunnel test section (Fig. 1b). The water vapor is driven out (at a discharge velocity $< 0.2 \text{ m s}^{-1}$) by an electric fan whose (vertical) momentum is mostly less than the friction velocity and is negligible compared with that of the prevailing flows (3 m s^{-1} to 6 m s^{-1}). Measurements show that the tracer transport is dominated by advection tracer flux (over 96%; Section 4.2.2). The results would not be affected too much though the discharge velocity is comparable to the friction velocity. Nevertheless, faster friction velocities and slower discharge velocities are worthy to be employed in future experiments. The water level in the tank is kept constant to facilitate a uniform water-consumption rate throughout the experiments (about 2 L an hour at room temperature and pressure). The tracer (water vapor) emission rate is in turn determined by the water-consumption rate during the experiments.

3.4. Measurement techniques

Velocities are probed by CT X-wire HWAs. The angle between the pair of X-wire is 100° to improve the accuracy of near-wall turbulence measurements because a larger angle could reduce the errors arising from inadequate yaw response in highly turbulent flows [16]. The

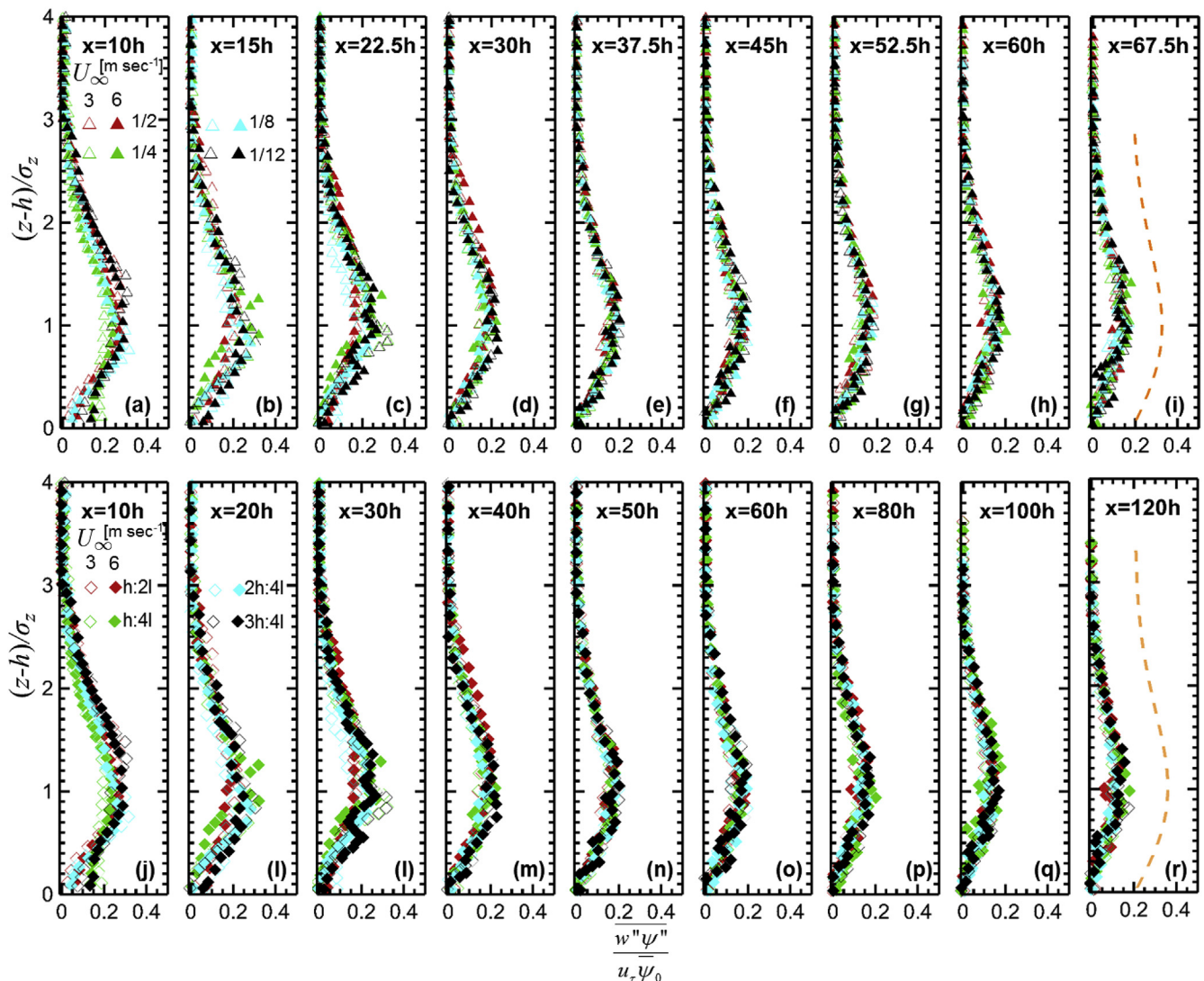


Fig. 9. Dimensionless turbulent tracer flux $\bar{w}''\psi''/u_\tau \bar{\psi}_0$, which is calculated by the Reynolds analogy Equation (4), over ribs (a to i) and bricks (j to r) plotted against dimensionless height $(z-h)/h$ at streamwise locations x . Orange dashed lines depict the theoretical variation (Equation (12)).

platinum-plated tungsten wires size 5×10^{-6} m in diameter on which a 2×10^{-3} -m-long sensing element is fabricated by copper electroplating. The analog output from the CT HWA is converted to digital by the 24-bit NI 9239 data acquisition module. Next, a LabVIEW program is used to collect the data via the NI cDAQ-9188 CompactDAQ chassis. The sampling frequency is 2 kHz and the data collection lasts for 50 s at each measurement point [63,64]. Equipment calibration is traceable following the scheme of the Institute of Sound and Vibration Research (ISVR) [65]. Besides, an in-house calibration comparing the wind speeds measured by the CT HWA with those by the Pitot tube installed in the wind tunnel is conducted beforehand in which the coefficient of determination is up to $R^2 = 0.9998$. The slope between the CT HWA and Pitot tube data is within 0.97–1.03, indicating that the measurement uncertainty is less than 3%. For the measurements of flow properties, seven vertical profiles are collected on the wind-tunnel center-plane ($y = 0$) over a repeating unit of roughness elements.

The vapor concentrations are detected by a pair of temperature and humidity SHT75 sensors (SENSIRION AG Switzerland). One is installed before the upstream section to monitor the background level while another samples the tracer concentrations in the urban plume. They are capacitive sensors measuring 0%–100% relative humidity (RH) at sensitivity of $\pm 1.5\%$ in temperature -40°C – 125°C . The RH φ

(57%–93% in the wind tunnel experiments) and temperature Θ (26°C – 31°C) are measured simultaneously to derive the vapor (mass) concentrations by the ideal gas law. The sensor response time is 8 s and the sampling duration is 50 s. A time delay of 20 s is applied to each sampling point, ensuring sufficient time for sensor response. The measurement uncertainty of vapor concentration, RH and temperature is 5%, 2% and 2%, respectively. The concentration profiles are measured at streamwise position x downstream of the emission source ($x = 0$) in the ranges of $10h \leq x \leq 67.5h$ for rib-type elements and $10h \leq x \leq 120h$ for brick-type elements. The sampling uniformity in the spanwise extent was tested beforehand whose spatial variation is less than 5% [66]. Detailed laboratory methodology is available elsewhere [19,33].

4. Results and discussion

4.1. Flows

In this section, the temporal $\bar{\phi}$ and spatial $\langle \phi \rangle$ averages are determined by averaging the data, respectively, during the sampling period at a single point and of the seven vertical profiles within a repeating unit of roughness element. The flow parameters are tabulated

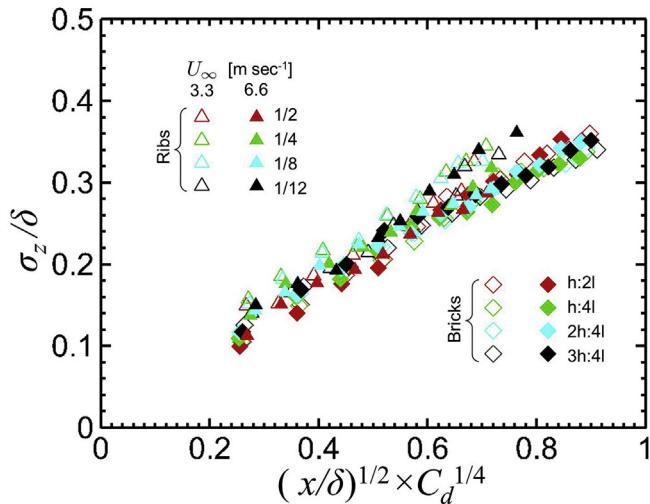


Fig. 10. Vertical dispersion coefficients σ_z expressed as functions of streamwise distance after the line source x over ribs and bricks. Here, C_d is the drag coefficient and δ the TBL thickness.

in Table 1. The TBL thickness δ is defined at the wall-normal distance where the spatio-temporal average of mean-wind speed is 99% of the freestream one, i.e. $\langle \bar{u} \rangle|_{z=\delta} = 0.99U_\infty$. The friction velocity u_τ is determined from the spatio-temporal average of momentum flux $\langle u''w'' \rangle$ near the wall. The zero-plane displacement height d and the roughness length z_0 are estimated by the best-fit regression of the mean-wind speed to the log-law.

4.1.1. Mean-wind-speed profiles

Vertical profiles of dimensionless mean-wind speed $\langle \bar{u} \rangle/U_\infty$ measured over arrays of roughness elements are compared in Fig. 3. The near-wall mean-wind speeds (at $z \approx h$) are about 35%–50% of the freestream ones. They increase gradually to $0.9U_\infty$ at 0.7δ in the outer layer that develops a major wind shear in the near-wall region. The mean-wind speeds exhibit the power-law profiles

$$\frac{\langle \bar{u} \rangle}{U_\infty} = \left(\frac{z - h}{\delta} \right)^n \quad (9)$$

which are commonly employed in boundary-layer meteorology. The exponent is found (empirically) in the range of $0.21 \leq n \leq 0.28$ that is comparable to the typical value over urban areas ($n = 0.25$) [67].

The dimensionless profiles of mean-wind speeds $\langle \bar{u} \rangle/u_\tau$ collapse on the logarithmic plot, suggesting the existence of the inertial sublayer (ISL; Fig. 4). The ISL thickness is shallow that shifts downward with increasing drag coefficient C_d or turbulence Reynolds number Re_τ , demonstrating the effect of aerodynamic resistance on the dynamics (in terms of d and z_0). Below the ISL, the mean-wind-speed profiles deviate notably from the theoretical log-law that is attributed to the roughness sublayer layer (RSL) effect as detailed elsewhere [68,69].

4.1.2. Turbulence profiles

Fig. 5 compares the fluctuating velocities $\langle u''u'' \rangle^{1/2}/u_\tau$ and turbulent momentum flux $\langle -u''w'' \rangle/u_\tau^2$ in a dimensionless manner. Generally, they collapse within narrow ranges that are independent from the wall roughness [68]. Close to the roughness elements, the streamwise ($2.2u_\tau \leq \langle u''u'' \rangle^{1/2} \leq 2.8u_\tau$) and vertical ($1.1u_\tau \leq \langle w''w'' \rangle^{1/2} \leq 1.2u_\tau$) fluctuating velocities are peaked at different extent that are comparable to those available in literature ($2.25u_\tau \leq \langle u''u'' \rangle^{1/2} \leq 2.75u_\tau$ and $1.01u_\tau \leq \langle w''w'' \rangle^{1/2} \leq 1.53u_\tau$) [69]. They generally increase with increasing drag coefficient and decrease with height, reducing gradually to 10% of the roof-level values at the TBL top. It is noteworthy that the vertical fluctuating velocity $\langle w''w'' \rangle^{1/2}$ exhibits different

behaviors over the two types of roughness elements. In the TBLs over the ribs, it increases with height that arrives an elevated, broad maximum ($\langle w''w'' \rangle^{1/2} \approx 1.1u_\tau$) within $0.1\delta \leq z-h \leq 0.2\delta$ then decreases gradually thereafter. On the contrary, the flows over the bricks show two types of maximum vertical fluctuating velocity. Elevated peaks of $\langle w''w'' \rangle^{1/2}$ are observed in the cases $2h:4l$ and $4h:4l$ (with additional LEGO® layers) but not $h:2l$ and $h:4l$ (bricks of the same height). It is because the flows over homogeneous roughness elements seldom descend into the street canyons for skimming or interference flow regimes so the peaks of vertical fluctuating velocity do not noticeably elevated [70]. The vertical profiles of turbulent momentum flux $\langle -u''w'' \rangle$ have a similar pattern over both ribs and bricks. They are about $0.7u_\tau^2 \leq \langle -u''w'' \rangle \leq 0.9u_\tau^2$ right over the roughness elements. The turbulent momentum flux increases with height, reaches the elevated peaks (close to unity) in $0.1\delta \leq z-h \leq 0.2\delta$, then decreases thereafter toward the TBL top. Turbulent momentum flux statistically represents the correlation between the streamwise and vertical velocity components so they are less correlated approaching the rough surfaces. The streamwise and vertical velocities decrease in the vicinity of roughness elements that also reduce the turbulent momentum flux. Properties measured at the two levels of mean-wind speeds are consistent, demonstrating the Reynolds-number independence for the results obtained in this paper.

4.2. Tracer plume

The tracer concentrations are sampled on the vertical centerplane of the wind tunnel. Unlike the flows, the tracer plume is inhomogeneous in the streamwise direction. Hence, only the temporal average of tracer concentrations $\bar{\psi}$ is reported in the following analyses.

4.2.1. Concentration profiles

Time-averaged tracer concentrations $\bar{\psi}$ are collected as functions of height along nine vertical transects (Fig. 6) at different streamwise locations $10h \leq x \leq 67.5h$ (ribs) and $10h \leq x \leq 120h$ (bricks). The upward growth of vertical plume spread in the streamwise direction after the line source is clearly captured. It is noteworthy that the crosswind plume spread widens with increasing drag coefficient such that the dimensionless tracer concentrations $\bar{\psi}/\bar{\psi}_0$ are bounded by the cases $AR = 1/2$ (smallest C_d) and $AR = 1/12$ (largest C_d) over the ribs. Here, the subscript 0 denotes the properties at the top of roughness elements. Likewise, the dimensionless tracer concentrations over the bricks are bounded by the cases $h:2l$ (smallest C_d) and $3h:4l$ (largest C_d). Hence, the plume dispersion is enhanced by the stronger turbulent mixing induced by the elevated aerodynamic resistance.

The plume spread can be quantified by the vertical dispersion coefficient

$$\sigma_z(x) = \left[\int_h^\delta z^2 \times \bar{\psi}(x, z) dz / \int_h^\delta \bar{\psi}(x, z) dz \right]^{1/2}. \quad (10)$$

It is also used to scale the height z for comparing the plume dispersion over different roughness elements in this paper. Among others, the dimensionless vertical profile of tracer concentrations $\bar{\psi}$ at $x = 60h$ serves as an example to illustrate the characteristic concentration distribution (Fig. 7). Although the data are collected over different roughness elements in a range of wind speeds, they exhibit the Gaussian form. Hence, the Gaussian model is a suitable candidate for the plume dispersion over homogeneous, urban areas provided that the dispersion coefficients are parameterized properly. However, a deviation is noted at $z \leq 0.5\sigma_z$. The wind-tunnel-measured tracer concentrations are overestimated up to 15% compared with those of the theoretical Gaussian model. Similar discrepancies have also been reported in previous wind tunnel experiments [17,24]. The elevated maximum tracer concentrations are attributed to the non-uniform mean-wind profiles, the strong turbulent mixing near the roughness elements and the (vertical) discharge momentum of the tracer source [33]. According to our

instrumentation record, the (upward) wind speed induced by the line source is $w_0 = 0.2 \text{ m s}^{-1}$. It is small (3%–6%) compared with the prevailing wind speed U_∞ (3.3 m s^{-1} or 6.6 m s^{-1}). The volumetric flux of air discharge from the line source is also small (0.1%) compared with the core flow. The water levels in the reservoir are the same throughout the experiments to ensure a constant emission rate of water vapor per unit length \dot{q} ($= 2.4 \pm 0.6 \text{ g m}^{-1} \text{ sec}^{-1}$). Based on the theory of rectangular jet of unit width, the initial plume rise induced by the discharge momentum from a line source in crossflows is in the order of 0.02 m – 0.04 m (h to $2h$) that is comparable to the elevated maximum concentration observed in the current wind tunnel experiments (Figs. 6 and 7). Comparing the friction velocity and discharge velocity is most appropriate to determine if the tracer emission is passive. Because of their similar magnitudes in this study, higher friction velocities would be tested in the future to reduce the initial plume rise.

4.2.2. Tracer fluxes

Streamwise advection tracer flux $\bar{u} \bar{\psi}$ is the product of the mean tracer concentrations (Equation (5)) and the mean-wind speeds (Equation (9)) whose analytical formulation is

$$\frac{\bar{u} \bar{\psi}}{U_\infty \bar{\psi}_0} = \left(\frac{z-h}{\delta} \right)^n \times \exp \left[-\frac{1}{2} \left(\frac{z-h}{\sigma_z} \right)^2 \right] \quad (11)$$

The freestream velocity U_∞ is used in the normalization of the advection tracer fluxes which are functions of $(z-h)/\delta$ and $(z-h)/\sigma_z$. It is noteworthy that, as shown previously, the mean-wind speed and the tracer concentrations follow the empirical power law and the Gaussian distribution, respectively. Equations (5) and (9) are thus the appropriate theoretical formulations used to derive Equation (11). Moreover, the advection tracer flux is peaked at $z = n^{1/2} \sigma_z$ theoretically. These theoretical transport characteristics are observed in the current wind-tunnel results as well (Fig. 8).

The advection tracer flux, which drives the tracer downstream horizontally, exhibits an alike pattern for all the cases being considered in the current wind tunnel experiments (Fig. 8). It increases from the TBL bottom with height, reaches the (local) maximum at $z = n^{1/2} \sigma_z$ then decreases thereafter. The experimental wind exponent n varies from 0.21 to 0.28. The corresponding theoretical elevation of maximum $\bar{u} \bar{\psi}/U_\infty \bar{\psi}_0$ is in the range of $0.46\sigma_z \leq z \leq 0.53\sigma_z$ that matches well with that observed in the experiments ($0.4\sigma_z \leq z \leq 0.7\sigma_z$). It is noted that the freestream velocity U_∞ is currently used as the characteristic velocity scale to normalize the advection tracer flux. The drag coefficient C_d is thus eliminated from Equation (11) and all the roughness effect is embedded in the vertical dispersion coefficient σ_z .

In favor of the anti-gradient diffusion model Equation (3) and the Reynolds analogy Equation (4), the theoretical dimensionless profile of vertical turbulent tracer flux $\bar{w}'\bar{\psi}'/u_\tau \bar{\psi}_0$ is in the form

$$\frac{\bar{w}'\bar{\psi}'}{u_\tau \bar{\psi}_0} \propto \left(\frac{\delta}{\sigma_z} \right) \times \left(\frac{z-h}{\sigma_z} \right) \times \exp \left[-\frac{1}{2} \left(\frac{z-h}{\sigma_z} \right)^2 \right]. \quad (12)$$

It is independent from the wind-profile exponent n (unlike the horizontal advection tracer flux Equation (11)) and the drag coefficient C_d . The dimensionless vertical turbulent tracer flux is peaked in the range of $0.9\sigma_z \leq z \leq 1.1\sigma_z$ in the experiments (Fig. 9) that agrees well with the theory ($z = \sigma_z$). It is however noteworthy that the dimensionless profiles of vertical turbulent tracer flux derived from Equation (3) are not fully independent from the streamwise position x . They are inversely related to the dispersion coefficient that are in turn inversely proportional to the streamwise position. It is thus expected that turbulent transport contributes more significantly in the near field for pedestrian-level pollutant removal. The contribution from the advection tracer flux to the total tracer flux is over 96% while the turbulent tracer flux is less than 4%. Besides, the turbulent tracer flux is positively correlated with the drag coefficient (correlation coefficient

$R > 0.8$) while the advection tracer flux is negative ($R > -0.8$). Dividing Equation (12) by Equation (11) yields

$$\frac{\bar{w}'\bar{\psi}'}{\bar{u} \bar{\psi}} \propto \frac{\delta^{n+1}}{\sigma_z^2} \times (z-h)^{1-n} \times \frac{u_\tau}{U_\infty} \quad (13)$$

that represents the analytical solution to the turbulent-tracer-flux-to-advection-tracer-flux ratio. It is in line with the experimental observation listed above.

4.3. Plume dispersion parameterization

Vertical dispersion coefficient σ_z is the key parameter in Gaussian models (Equation (5)). Practically, it is parameterized empirically by atmospheric stability in term of the distance behind the pollutant source [3,46–48]. This approach has been well received by the industry as well as regulatory enactment for decades, which, however, does not account for the effect of surface feature in particular sizeable roughness elements such as urban morphology. The Monin–Obukhov similarity theory (MOST) shows that mechanical wind shear dominates ASL turbulence generation rather than atmospheric stability in the vicinity to land surfaces. Our previous study [33] suggested the linear correlation between σ_z and the fourth root of drag coefficient $C_d^{1/4}$ or the square root of u_τ (Equation (8)) that is supported by the current experimental data (Fig. 10). The results obtained from the two types of roughness element exhibit a close correlation (coefficient of determination $R^2 = 0.92$). These results collectively demonstrate that the drag coefficient C_d (or the friction velocity u_τ) is able to parameterize the aerodynamic effect of (rough) urban areas on plume dispersion in isothermal conditions. Apart from using the friction velocity, this new formulation possesses the advantage that the full spectra of flow details are no longer necessary in practical modelling exercises. Moreover, it is applicable to different types of roughness element regardless of the shape, size and orientation. Wind tunnel measurements with advanced instrumentation for more complicated, realistic urban morphology will be conducted to further verify the functionality of Equation (8).

5. Conclusions

Laboratory wind tunnel experiments of plume dispersion over reduced-scale, idealized urban models are conducted. Eight configurations of hypothetical urban areas fabricated by ribs (AR = 1/2, 1/4, 1/8, and 1/12) and bricks ($h:2l$, $h:4l$; $2h:4l$, and $3h:4l$) are used to model the TBLs for drag coefficient C_d varying from 4.7×10^{-3} to 10×10^{-3} (equivalent to $0.048 \leq u_\tau/U_\infty \leq 0.071$). The mean-wind speeds $\langle \bar{u} \rangle$, compared with the freestream ones U_∞ , are reduced by 50%–65% over the roughness elements. On the other hand, the turbulence components (streamwise and vertical fluctuating velocities $\langle \bar{u}'\bar{u}' \rangle^{1/2}$ and momentum flux $\langle -\bar{u}'\bar{v}' \rangle$) are substantially enhanced. The dimensionless profiles of tracer concentration $\bar{\psi}/\bar{\psi}_0$ exhibit the theoretical Gaussian form though the maximum concentrations are elevated mildly (h to $2h$ probably due to the vertical discharge momentum at the line source). In particular, both analytical and experimental results demonstrate that the (conventional) Gaussian models is an appropriate candidate of plume parameterization provided that the dispersion coefficient σ_z is calibrated properly. Roughness promotes momentum flux that in turn enhances pollutant removal from pedestrian level. It is also demonstrated by the proportionality between the turbulent tracer flux and friction velocity (Equation (12)). The advection tracer flux $\bar{u} \bar{\psi}$ is found peaked at $0.4\sigma_z$ to $0.7\sigma_z$ while the turbulent tracer flux $\bar{w}'\bar{\psi}'$ at $0.9\sigma_z$ to $1.1\sigma_z$ that are in line with the theory. It is also found that the advection (turbulent) tracer flux increases (decreases) with increasing drag coefficient (correlation coefficient R over 0.8). Hence, urban roughness enhances turbulent transport and subsequently the plume dispersion. A robust parameterization of vertical dispersion coefficient σ_z ($\propto x^{1/2} \times \delta^{1/2} \times C_d^{1/4}$) is verified by the current wind tunnel measurements (of hypothetical, homogeneous, urban areas) that is applicable to full

spectra of building configuration. In view of the tight correlation between plume spread and the aerodynamic resistance of urban areas, proper architectural design and urban planning, such as increasing the drag in building or neighborhood scales, could be the alternative solutions to improve pedestrian-level air quality.

Acknowledgements

The authors are grateful to the Hong Kong (HK) Research Grants Council (RGC) for the support through General Research Fund (GRF) 17250616 as well as the insightful comment raised by the four anonymous reviewers.

References

- [1] B. Brunekreef, S.T. Holgate, Air pollution and health, *The Lancet* 360 (2002) 1233–1242.
- [2] J. Lelieveld, J.S. Evans, M. Fnais, D. Giannadaki, A. Pozzer, The contribution of outdoor air pollution sources to premature mortality on a global scale, *Nature* 525 (2015) 367.
- [3] S.P. Arya, *Air Pollution Meteorology and Dispersion*, Oxford University Press, Cambridge, U.K, 1999.
- [4] Geneva: WHO, WHO air quality guidelines for particulate matter, ozone, nitrogen dioxide and sulfur dioxide, Global Update 2005. Summary of Risk Assessment, 2006 WHO/SDE/PHE/OEH/06.02 http://apps.who.int/eproxy2.lib.hku.hk/iris/bitstream/10665/69477/1/WHO_SDE_PHE_OEH_06.02_eng.pdf.
- [5] C.K. Chan, X. Yao, Air pollution in mega cities in China, *Atmos. Environ.* 42 (2008) 1–42.
- [6] C.M. Wong, N. Vichit-Vadakan, H. Kan, Z. Qian, Public health and air pollution in Asia (PAPA): a multicity study of short-term effects of air pollution on mortality, *Environ. Health Perspect.* 116 (2008) 1195–1202.
- [7] T.N.H. Chung, C.-H. Liu, On the mechanism of air pollutant removal in two-dimensional idealized street canyons: a large-eddy simulation approach, *Boundary-Layer Meteorol.* 148 (2013) 241–253.
- [8] C.-H. Liu, C.C.C. Wong, On the pollutant removal, dispersion, and entrainment over two-dimensional idealized street canyons, *Atmos. Res.* 135/136 (2014) 128–142.
- [9] J. Jiménez, Turbulent flows over rough walls, *Annu. Rev. Fluid Mech.* 36 (2004) 173–196.
- [10] E. Ng, Policies and technical guidelines for urban planning of high-density cities – air ventilation assessment (AVA) of Hong Kong, *Build. Environ.* 44 (2009) 1478–1488.
- [11] P. de Haan, M.W. Rotach, M. Werfeli, Modification of an operational dispersion model for urban applications, *J. Appl. Meteorol.* 40 (2001) 864–879.
- [12] R.E. Britter, S.R. Hanna, Flow and dispersion in urban areas, *Annu. Rev. Fluid Mech.* 35 (2003) 469–496.
- [13] M. Lateb, R.N. Meroney, M. Yataghene, H. Fellouah, F. Saleh, M.C. Boufadel, On the use of numerical modelling for near-field pollutant dispersion in urban environments – A review, *Environ. Pollut.* 208 (Part A) (2016) 271–283.
- [14] Y. Zhang, K.C.S. Kwok, X.P. Liu, J.L. Niu, Characteristics of air pollutant dispersion around a high-rise building, *Environ. Pollut.* 204 (2015) 280–288.
- [15] K. Ahmad, M. Khare, K.K. Chaudhry, Wind tunnel simulation studies on dispersion at urban street canyons and intersections — a review, *J. Wind Eng. Ind. Aerodyn.* 93 (2005) 697–717.
- [16] A.E. Perry, K.L. Lim, S.M. Henbest, An experimental study of the turbulence structure in smooth- and rough-wall boundary layers, *J. Fluid Mech.* 177 (1987) 437–466.
- [17] P. Salizzoni, R. Van Lierferinge, L. Soulhac, P. Mejean, R.J. Perkins, Influence of wall roughness on the dispersion of a passive scalar in a turbulent boundary layer, *Atmos. Environ.* 43 (2009) 734–748.
- [18] S.A. Zaki, A. Hagishima, J. Tanimoto, N. Ikegaya, Aerodynamic parameters of urban building arrays with random geometries, *Boundary-Layer Meteorol.* 138 (2011) 99–120.
- [19] Y.K. Ho, C.-H. Liu, A wind tunnel study of flows over idealised urban surfaces with roughness sublayer corrections, *Theor. Appl. Climatol.* 130 (2017) 305–320.
- [20] P. Salizzoni, L. Soulhac, P. Mejean, R.J. Perkins, Influence of a two-scale surface roughness on a neutral turbulent boundary layer, *Boundary-Layer Meteorol.* 127 (2008) 97–110.
- [21] H. Cheng, P. Hayden, A.G. Robins, I.P. Castro, Flow over cube arrays of different packing densities, *J. Wind Eng. Ind. Aerodyn.* 95 (2007) 715–740.
- [22] A. Hagishima, J. Tanimoto, K. Nagayama, S. Meno, Aerodynamic parameters of regular arrays of rectangular blocks with various geometries, *Boundary-Layer Meteorol.* 132 (2009) 315–337.
- [23] M. Placidi, B. Ganapathisubramani, Effects of frontal and plan solidities on aerodynamic parameters and the roughness sublayer in turbulent boundary layers, *J. Fluid Mech.* 782 (2015) 541–566.
- [24] R.W. Macdonald, R.F. Griffiths, D.J. Hall, A comparison of results from scaled field and wind tunnel modelling of dispersion in arrays of obstacles, *Atmos. Environ.* 32 (1998) 3845–3862.
- [25] A.F. Mohammad, S.A. Zaki, A. Hagishima, M.S.M. Ali, Determination of aerodynamic parameters of urban surfaces: methods and results revisited, *Theor. Appl. Climatol.* 122 (2015) 635–649.
- [26] P. Huq, A. Rahman, A, Optimizing the determination of roughness parameters for model urban canopies, *Boundary-Layer Meteorol.* 168 (2018) 497–515.
- [27] C.W. Kent, S. Grimmond, J. Barlow, D. Gatey, S. Kotthaus, F. Lindberg, C.H. Halios, Evaluation of urban local-scale aerodynamic parameters: implications for the vertical profile of wind speed and for source areas, *Boundary-Layer Meteorol.* 164 (2017) 183–213.
- [28] M. Carpentieri, A.G. Robins, P. Hayden, E. Santi, Mean and turbulent mass flux measurements in an idealised street network, *Environ. Pollut.* 234 (2018) 356–367.
- [29] Š. Nosek, L. Kukačka, R. Kellnerová, K. Jurčáková, Z. Jaňour, Ventilation processes in a three-dimensional street canyon, *Boundary-Layer Meteorol.* 159 (2016) 259–284.
- [30] Y. Tominaga, B. Blocken, Wind tunnel experiments on cross-ventilation flow of a generic building with contaminant dispersion in unsheltered and sheltered conditions, *Build. Environ.* 92 (2015) 452–461.
- [31] F. Paschke, J.F. Barlow, A. Robins, Wind-tunnel modelling of dispersion from a scalar area source in urban-like roughness, *Boundary-Layer Meteorol.* 126 (2008) 103–124.
- [32] A. Robins, I. Castro, P. Hayden, N. Steggel, D. Contini, D. Heist, A wind tunnel study of dense gas dispersion in a neutral boundary layer over a rough surface, *Atmos. Environ.* 35 (2001) 2243–2252.
- [33] Z. Mo, C.-H. Liu, Wind tunnel measurements of pollutant plume dispersion over hypothetical urban areas, *Build. Environ.* 132 (2018) 357–366.
- [34] A. Ricci, M. Burlando, A. Freda, M.P. Repetto, Wind tunnel measurements of the urban boundary layer development over a historical district in Italy, *Build. Environ.* 111 (2017) 192–206.
- [35] P. Kastner-Klein, M.W. Rotach, Mean flow and turbulence characteristics in an urban roughness sublayer, *Boundary-Layer Meteorol.* 111 (2004) 55–84.
- [36] N. Antoniou, H. Montazeri, H. Wigo, M.K.A. Neophytou, B. Blocken, M. Sandberg, CFD and wind-tunnel analysis of outdoor ventilation in a real compact heterogeneous urban area: evaluation using “air delay”, *Build. Environ.* 126 (2017) 355–372.
- [37] S.E. Belcher, Mixing and transport in urban areas, *Phil. Trans. R. Soc. A* 363 (2005) 2947–2968.
- [38] A.E. Perry, W.H. Schofield, P.N. Joubert, Rough wall turbulent boundary layers, *J. Fluid Mech.* 37 (1969) 383–413.
- [39] J.H. Spurk, *Fluid Mechanics*, Springer-Verlag, Berlin, Heidelberg, 1997.
- [40] R. Wahidi, W. Chakroun, S. Al-Fahed, The behavior of the skin-friction coefficient of a turbulent boundary layer flow over a flat plate with differently configured transverse square grooves, *Exp. Therm. Fluid Sci.* 30 (2005) 141–152.
- [41] M.R. Raupach, R.A. Antonia, S. Rajagopalan, Rough-wall turbulent boundary layers, *Appl. Mech. Rev.* 44 (1991) 1–25.
- [42] Y.K. Ho, C.-H. Liu, M.S. Wong, Preliminary study of the parameterisation of street-level ventilation in idealised two-dimensional simulations, *Build. Environ.* 89 (2015) 345–355.
- [43] C.-H. Liu, C.T. Ng, C.C.C. Wong, A theory of ventilation estimate over hypothetical urban areas, *J. Hazard Mater.* 296 (2015) 9–16.
- [44] Y.K. Ho, C.-H. Liu, Street-level ventilation in hypothetical urban areas, *Atmosphere* 8 (2017) 124.
- [45] M. Carpentieri, P. Hayden, A.G. Robins, Wind tunnel measurements of pollutant turbulent fluxes in urban intersections, *Atmos. Environ.* 46 (2012) 669–674.
- [46] F. Pasquill, F.B. Smith, *Atmospheric Diffusion*, 3rd., Wiley, New York, 1983.
- [47] D.B. Turner, *Workbook of Atmospheric Dispersion Estimates: an Introduction to Dispersion Modeling*, Lewis Publishers, London, UK, 1994.
- [48] G.A. Briggs, *Diffusion Estimation for Small Emissions*, ATDL, NOAA/ARL, Oak Ridge, TN 37830, 1973, p. 23. ATDL Report No. 79.
- [49] S.R. Hanna, R. Britter, P. Franzese, A baseline urban dispersion model evaluated with Salt Lake City and Los Angeles tracer data, *Atmos. Environ.* 37 (2003) 5069–5082.
- [50] S. Hanna, E. Baja, A simple urban dispersion model tested with tracer data from Oklahoma City and Manhattan, *Atmos. Environ.* 43 (2009) 778–786.
- [51] J.C. Weil, Updating applied diffusion models, *J. Appl. Meteorol. Climatol.* 24 (1985) 1111–1130.
- [52] A. Venkatram, Vertical dispersion of ground-level releases in the surface boundary layer, *Atmos. Environ.* 26 (1992) 947–949.
- [53] USEPA, User's Guide for the Industrial Source Complex (ISC3) Dispersion Models, Volume II – Description of Model Algorithms, U.S. Environmental Protection Agency, Office of Air Quality Planning and Standards Emissions, Monitoring, and Analysis Division, Research Triangle Park, North Carolina 27711, 1995 EPA-454/B-95-003b.
- [54] A.J. Cimorelli, S.G. Perry, A. Venkatram, J.C. Weil, R.J. Paine, R.B. Wilson, R.F. Lee, W.D. Peters, R.W. Brode, AERMOD: a dispersion model for industrial source applications. Part I: general model formulation and boundary layer characterization, *J. Appl. Meteorol.* 44 (2005) 682–693.
- [55] CERC, ADMS-urban User Guide, Cambridge Environmental Research Consultants, 2017.
- [56] J.S. Scire, G.S. David, J.Y. Robert, Model Formulation and User's Guide for the CALPUFF Dispersion Model, California Air Resources Board, Sacramento, California, 1990, p. 95814 Report No. AC25-2.
- [57] L. Soulhac, P. Salizzoni, F.-X. Cierco, R.J. Perkins, The model SIRANE for atmospheric urban pollutant dispersion: Part I: presentation of the model, *Atmos. Environ.* 45 (2011) 7379–7395.
- [58] L. Soulhac, P. Salizzoni, P. Mejean, D. Didier, I. Rios, The SIRANE model for atmospheric urban pollutant dispersion: Part II, validation of the model on a real case study, *Atmos. Environ.* 49 (2012) 320–337.
- [59] K.L. Calder, Some recent British work on the problems of diffusion in the lower atmosphere, *Proceedings of the US Technique Conference Air Pollution*, vol. 787,

- McGraw- Hill, New York, US, 1952.
- [60] Z. Mo, C.-H. Liu, A wind tunnel study of ventilation mechanism over hypothetical urban roughness: the role of intermittent motion scales, *Build. Environ.* 135 (2018) 94–103.
 - [61] K.K. Leung, C.-H. Liu, Local mass transfer coefficient over idealised two-dimensional urban street canyons, *Int. J. Environ. Pollut.* 50 (2012) 75–82.
 - [62] K.K. Leung, C.-H. Liu, C.C.C. Wong, J.C.Y. Lo, G.C.T. Ng, On the study of ventilation and pollutant removal over idealized two-dimensional urban street canyons, *Build. Simul.* 5 (2012) 359–369.
 - [63] H. Cheng, I.P. Castro, Near-wall flow development after a step change in surface roughness, *Boundary-Layer Meteorol.* 105 (2002) 411–432.
 - [64] H. Cheng, I.P. Castro, Near wall flow over urban-like roughness, *Boundary-Layer Meteorol.* 104 (2002) 229–259.
 - [65] H. Bruun, Interpretation of a hot wire signal using a universal calibration law, *J. Phys. E Sci. Instrum.* 4 (1971) 225.
 - [66] Y.K. Ho, reportWind-Tunnel Study of Turbulent Boundary Layer over Idealized Urban Roughness with Application to Urban Ventilation Problem. PhD Dissertation, Department of Mechanical Engineering, The University of Hong Kong.
 - [67] R. Barratt, *Atmospheric Dispersion Modelling: an Introduction to Practical Application*, Earthscan Publication, London, 2001.
 - [68] M.R. Raupach, Conditional statistics of Reynolds stress in rough-wall and smooth-wall turbulent boundary layers, *J. Fluid Mech.* 108 (1981) 363–382.
 - [69] M. Roth, Review of atmospheric turbulence over cities, *Q. J. Roy. Meteorol. Soc.* 126 (2000) 941–990.
 - [70] K. Nourmohammadi, P.K. Hopke, J.J. Stukel, Turbulent air flow over rough surfaces: II. turbulent flow parameters, *J. Fluids Eng.* 107 (1985) 55–60.